Received: 28 December 2023 | Revised: 5 June 2024 | Accepted: 24 June 2024

DOI: 10.1002/mrm.30216

RESEARCH ARTICLE

Magnetic Resonance in Medicine

Rapid submillimeter QSM and R_2* mapping using interleaved multishot 3D-EPI at 7 and 3 Tesla

Rüdiger Stirnberg[1] | **Andreas Deistung**[2] | **Jürgen R. Reichenbach**[3] | **Monique M. B. Breteler**[4,5] | **Tony Stöcker**[1,6]

[1]MR Physics, German Center for Neurodegenerative Diseases (DZNE), Bonn, Germany

[2]Clinic and Outpatient Clinic for Radiology, University Hospital Halle (Saale), University Medicine Halle, Halle (Saale), Germany

[3]Medical Physics Group, Institute of Diagnostic and Interventional Radiology, Jena University Hospital, Jena, Germany

[4]Population Health Sciences, German Center for Neurodegenerative Diseases (DZNE), Bonn, Germany

[5]Faculty of Medicine, Institute for Medical Biometry, Informatics and Epidemiology (IMBIE), University of Bonn, Bonn, Germany

[6]Department of Physics and Astronomy, University of Bonn, Bonn, Germany

Correspondence
Rüdiger Stirnberg, German Center for Neurodegenerative Diseases (DZNE), MR Physics, Venusberg-Campus 1, Building 99, 53127 Bonn, Germany.
Email: ruediger.stirnberg@dzne.de

Abstract

Purpose: To explore the high signal-to-noise ratio (SNR) efficiency of interleaved multishot 3D-EPI with standard image reconstruction for fast and robust high-resolution whole-brain quantitative susceptibility (QSM) and R_2^* mapping at 7 and 3T.

Methods: Single- and multi-TE segmented 3D-EPI is combined with conventional CAIPIRINHA undersampling for up to 72-fold effective gradient echo (GRE) imaging acceleration. Across multiple averages, scan parameters are varied (e.g., dual-polarity frequency-encoding) to additionally correct for B_0-induced artifacts, geometric distortions and motion retrospectively. A comparison to established GRE protocols is made. Resolutions range from 1.4 mm isotropic (1 multi-TE average in 36 s) up to 0.4 mm isotropic (2 single-TE averages in approximately 6 min) with whole-head coverage.

Results: Only 1-4 averages are needed for sufficient SNR with 3D-EPI, depending on resolution and field strength. Fast scanning and small voxels together with retrospective corrections result in substantially reduced image artifacts, which improves susceptibility and R_2^* mapping. Additionally, much finer details are obtained in susceptibility-weighted image projections through significantly reduced partial voluming.

Conclusion: Using interleaved multishot 3D-EPI, single-TE and multi-TE data can readily be acquired 10 times faster than with conventional, accelerated GRE imaging. Even 0.4 mm isotropic whole-head QSM within 6 min becomes feasible at 7T. At 3T, motion-robust 0.8 mm isotropic whole-brain QSM and R_2^* mapping with no apparent distortion in less than 7 min becomes clinically feasible. Stronger gradient systems may allow for even higher effective acceleration rates through larger EPI factors while maintaining optimal contrast.

KEYWORDS

3D-EPI, CAIPIRINHA, QSM, R_2^* mapping, ultra-high field

1 | INTRODUCTION

Quantitative susceptibility mapping (QSM) and mapping of the effective transverse relaxation rate ($R_2^* = 1/T_2^*$) provide valuable quantitative information about biological tissue in vivo. For instance, voxel-wise information on magnetic susceptibility, χ, and R_2^* allows drawing spatially resolved conclusions on deep gray matter iron content[1,2] and white matter myelination.[3] Using χ and R_2^* together even allows separating the two sources on a subvoxel level.[4–6]

Magnitude and phase MR images for R_2^* mapping and QSM are usually acquired using volumetric (3D) spoiled gradient echo (GRE) imaging. Often, relatively short repetition times ($TR \ll T_2$) are combined with low flip angle excitations to maximize signal for the longitudinal relaxation time (T_1) of a specific tissue. Within each TR, a different phase-encoded k-space line is acquired using a frequency-encoding gradient pulse.

For optimal R_2^* and susceptibility contrast, the echo time (TE) should be on the order of the average tissue T_2^*. For R_2^* mapping, a reasonable range of short-to-long TEs should be sampled. Both result in rather long TR and, depending on the desired voxel size, can lead to very long acquisition times (TA) and related artifacts (motion, field fluctuations, etc.), even with state-of-the-art imaging acceleration supported by most scanner vendors (e.g., SENSE,[7] GRAPPA[8] or CAIPIRINHA[9]). Otherwise, typical compromises to shorten TA include anisotropic voxels, reduced slab coverage in slice direction or the use of shorter, but suboptimal TE and TR.

Previous work has used echo planar imaging (EPI) to acquire GRE data more efficiently for rapid QSM (e.g., 2D-EPI,[10] 3D-EPI,[11,12] or 3D planes-on-a-paddlewheel[13]). Such approaches, however, did not consider multishot segmentation or relied only on single-TE acquisitions, preventing high-resolutions and multi-TE QSM or R_2^* mapping. On the other hand, interleaved multishot 3D-EPI has already been utilized successfully for high-resolution T_2^*- and susceptibility-weighted imaging as well as multiparametric mapping, including R_2^* mapping, at 3T and 7T.[14–16] Such approaches combined with QSM have vast neuroscientific potential (e.g., Reference 17).

In this work, we first determine the signal-to-noise ratio (SNR) efficiency benefit of segmented 3D-EPI using longer TRs over typical 3D-GRE.[15] We then show that combining R-fold CAIPIRINHA undersampling with an EPI factor $N > 1$ allows for significant imaging acceleration (up to $N \times R$-fold) using vendor-provided image reconstruction. This makes simple, retrospective image-based corrections (e.g., for motion) between repeated measurements feasible that improve the final average magnitude and phase substantially, thus paving the way to routine T_2^*-weighted imaging at ultra-high isotropic resolutions. We demonstrate particularly efficient whole-head QSM and R_2^* mapping using single-TE and multi-TE interleaved multi-shot 3D-EPI at 7T and 3T with isotropic resolutions as high as 400 microns.

2 | THEORY

2.1 | SNR efficiency of gradient echo imaging

In Appendix A it is shown that steady-state GRE imaging (of a monoexponential free induction decay) is most SNR-efficient, when the Ernst angle is used and the signal is sampled throughout a particularly long TR (Equation A5):

$$TR_{opt} \approx 1.256T_2^* + \delta_0 + \delta_1.$$

Here, δ_0 and δ_1 denote void times before and after signal sampling, respectively (see Figure A1A,B,D). A long TR is beneficial for acquisitions with rather long TE as required for optimal T_2^*- and susceptibility-weighting. If signal acquisition is split throughout the TR (e.g., multi-echo GRE or EPI, see Figure A1A,C,E), the SNR-optimal TR becomes even longer, according to Appendix B. In both cases, however, SNR efficiency drops relatively quickly, when shorter TRs are used (see Figure 1).

While there are different ways to implement single- or multi-echo 3D-GRE with long TR in practice, a single phase-encoding step per TR and TE typically results in long TA.

However, when using multishot 3D-EPI, TA reduces by the EPI factor, a.k.a. echo train length, N. While SNR is approximately reduced by $1/\sqrt{N}$ compared to an equivalent single-TE GRE (approximately N-fold increased frequency-encode bandwidth), SNR efficiency is still as high. This means that approximately the same SNR can be regained by acquiring and averaging N (complex-valued) images in the same TA.

Depending on the application, the SNR of $M < N$ averages may already suffice and TA would be only a fraction M/N compared to the TR-matched 3D-GRE. If the 3D-GRE uses a much shorter TR than TR_{opt}, sufficient SNR can even be gained in much shorter TA using 3D-EPI with $TR \approx TR_{opt}$. For this strategy, it typically makes sense to chose N as large as possible, that is, maximize frequency-encode bandwidth (minimize echo spacing, ESP) and chose the largest EPI factor that fits into TR

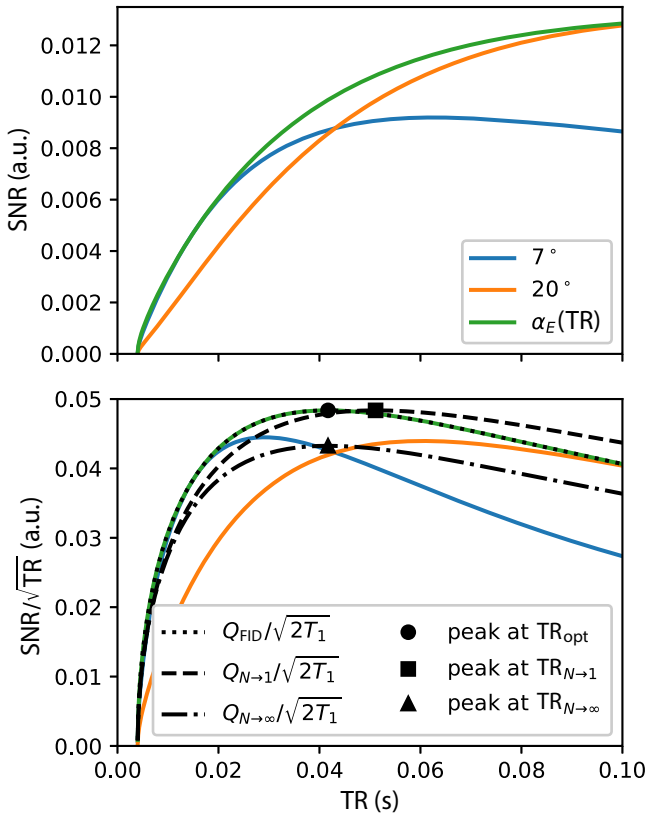

FIGURE 1 Signal-to-noise ratio (SNR) (top) and SNR efficiency (bottom) of spoiled GRE as a function of repetition time (TR) for different flip angles (solid lines) and the Ernst angle (α_E(TR)) assuming $T_1 = 2.0$ s and $T_2^* = 30$ ms. Bottom: approximated efficiency curves and peaks for a single FID (dotted) and the extremal cases of the multi(N)-echo model (dashed: $N \to 1$, dash-dotted: $N \to \infty$). All curves are only defined for TR > 4 ms (the sequence void time assumed here, e.g. for phase-encoding). The multi-echo model assumes that a fraction of the overall sampling window (here: 20%) is not sampled.

while meeting TE at the k-space center line (see single-TE EPI experiments below).

2.2 | Interleaved multishot 3D-EPI

Taking advantage of its high SNR efficiency, an interleaved multishot 3D-EPI sequence with CAIPIRINHA sampling[9,18] is considered in this work for maximum acceleration capabilities along the primary and secondary phase-encode directions (y and z w.l.o.g.). Using moderately high parallel imaging undersampling, $R_y \cdot R_z \leq 6$, and a small number of averages, M, still quite high effective acceleration rates can be achieved using a large EPI factor, N:

$$R_{\text{eff}} = R_y \cdot R_z \cdot N/M.$$

Susceptibility- and T_2^*-induced artifacts along the frequency-encode direction (x, w.l.o.g.) are negligible as very high bandwidths are typically used. The interleaved EPI readout results in a steady, but lower bandwidth along y. Still, with high segmentation (S), actual phase-encode bandwidths,

$$\text{BW}_y\ [\text{Hz/mm}] = \frac{S \cdot R_y}{\text{ESP}\ [\text{s}] \cdot \text{FoV}_y\ [\text{mm}]},$$

become close to the frequency-encode bandwidths of typical GRE protocols (cf. Table 1). Here, FoV_y refers to the phase-encode field-of-view. Therefore, GRE-typical geometric distortions and "T_2^* blurring" can be expected, however along y.

Finally, by adding phase-encode rephasers regularly between every few EPI echoes, a multi-TE EPI readout is implemented[16] that trades multi-echo information for TA, but still performs at comparable SNR efficiency (see fast multi-TE experiment below). If sufficiently short multi-TE EPI readouts cannot be realized with a practical EPI factor, we utilize "jittered" TEs across measurements (see high-resolution multi-TE experiments below).

2.3 | Retrospective corrections and dual-polarity frequency-encoding

Unlike a single, long 3D-GRE acquisition, retrospective image-based corrections can be performed across M rapid 3D-EPI acquisitions. For instance, coregistration (inter-volume motion correction) can be performed before averaging. Likewise, local phase changes over time (e.g., due to frequency drift or motion) can be matched before averaging. If the phase encode polarity is changed for at least one measurement, it is also possible to estimate and correct geometric distortions along the phase-encode direction before averaging.

Another option is to invert the EPI frequency-encode polarity in every other scan (dual-polarity frequency-encoding). When reordered, hypothetically, two complete sets of cohesive, single-polarity k-space data according to Figure 2C,D could be obtained from two EPI measurements according to Figure 2A,B: one acquired with only positive (red lines, $C(\boldsymbol{k})$) and one with only negative frequency-encode polarity (blue lines, $D(\boldsymbol{k})$). The two corresponding images, $\hat{C}(\boldsymbol{r})$ and $\hat{D}(\boldsymbol{r})$, would, for instance, not suffer from Nyquist ghosts, even if acquired with a systematic k_x shift between positive and negative lines. If navigator-based phase correction were already performed, as in this work, the residual phase discrepancy would become negligible: The k-space data could be averaged to yield a high-SNR image without Nyquist ghosts.

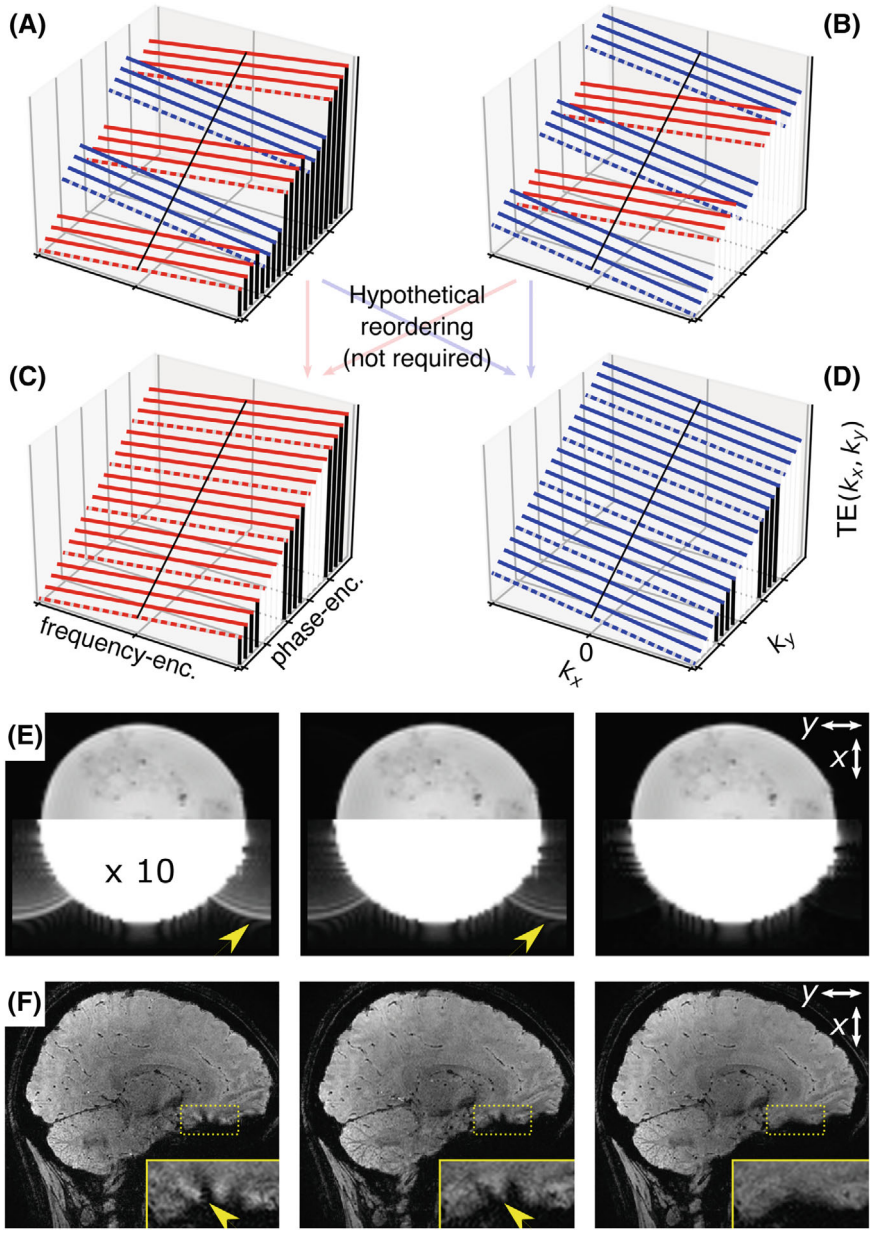

FIGURE 2 Echo time (TE ~ phase error) vs. $k_x \times k_y$ for original dual-polarity acquisition (A,B) and hypothetical reordering (C,D) of interleaved multi-shot echo planar imaging with echo time shifting ($S = 4$, $N = 5$, dashed: first interleave, red/blue: pos./neg. frequency-encoding polarity). Mitigated Nyquist ghosts (E) and segmentation artifacts (F) after dual-polarity averaging of images according to (A,B). Spherical phantom intensities scaled by a factor of 10 show low-intensity Nyquist ghosts before averaging (E, 3T, no segmentation, standard reconstruction). Magnified insets in (F) show complementary segmentation artifacts before averaging and a reduced, homogeneous dropout area after averaging (7T, $N = 12$, $S = 9$, $3 \times 2_{z1}$, "IcePAT" reconstruction). x: frequency-encode, y: phase-encode.

2.3.1 | Mitigation of segmentation artifacts

More importantly, in this work, we propose dual-polarity frequency-encoding to mitigate off-resonance-induced segmentation artifacts in interleaved multi-shot EPI, as demonstrated in Figure 2F and as shown by numerical simulations in Figure S1-2 for varying EPI factors. These are caused by a polarity-dependent k_x phase tilt, rather than systematic k_x shifts (e.g., due to eddy currents). While echo time shifting (ETS)[19] is already implemented for a smooth, linear TE evolution along k_y at $k_x = 0$, phase jumps still remain between echo sections (contiguous red and blue sections in Figure 2A,B) for all $k_x \neq 0$. The two hypothetical images $\hat{C}(\boldsymbol{r})$ and $\hat{D}(\boldsymbol{r})$, on the other hand, would be free of segmentation artifacts. An off-resonant voxel would only be displaced in opposite directions along x according to the k_x phase tilt. With large frequency-encode bandwidths, as used in EPI, the displacements are usually well below the nominal voxel size for typical off-resonance frequencies in the brain. Consequently, averaging the two reordered k-space sets would yield an image free of segmentation artifacts. Blurring along x would occur only where voxels are extremely off-resonant (cf. Figure S1).

2.3.2 | Dual-polarity averaging

As the Fourier transform between k-space and image space ($\mathcal{F}^{-1}$) is linear, Nyquist ghosts and segmentation artifacts

can be mitigated as described without the need to reorder positive and negative frequency-encode lines of the original k-space data $A(\boldsymbol{k})$ and $B(\boldsymbol{k})$ according to Figure 2A,B:

$$\begin{aligned}\frac{1}{2}[\hat{C}(\boldsymbol{r})+\hat{D}(\boldsymbol{r})] &= \frac{1}{2}\left[\mathcal{F}^{-1}\{C(\boldsymbol{k})\}+\mathcal{F}^{-1}\{D(\boldsymbol{k})\}\right] \\ &= \frac{1}{2}\mathcal{F}^{-1}\{C(\boldsymbol{k})+D(\boldsymbol{k})\} \\ &= \frac{1}{2}\mathcal{F}^{-1}\{A(\boldsymbol{k})+B(\boldsymbol{k})\} \quad .\end{aligned}$$

Averaging can furthermore be performed in the image domain instead of the k-space domain:

$$\begin{aligned}\frac{1}{2}\mathcal{F}^{-1}\{A(\boldsymbol{k})+B(\boldsymbol{k})\} &= \frac{1}{2}\left[\mathcal{F}^{-1}\{A(\boldsymbol{k})\}+\mathcal{F}^{-1}\{B(\boldsymbol{k})\}\right] \\ &= \frac{1}{2}[\hat{A}(\boldsymbol{r})+\hat{B}(\boldsymbol{r})] \quad .\end{aligned}$$

From two complex-valued dual-polarity images $\hat{A}(\boldsymbol{r})$ and $\hat{B}(\boldsymbol{r})$ with residual Nyquist ghosts and segmentation artifacts, one dual-polarity average (DPA) image with eliminated Nyquist ghosts and mitigated segmentation artifacts is obtained, as demonstrated in Figure 2E,F.

3 | METHODS

3.1 | Experiments

A custom skipped-CAIPI 3D-EPI (SC-EPI) sequence[18] that optionally inverts the frequency-encode polarity in every other measurement, was implemented at 7T (Siemens Healthineers, MAGNETOM 7TPlus) and at 3T (MAGNETOM Prisma). Both scanners are equipped with a high-performance gradient system (70 mT/m, 200 T/m/s at 7T; 80 mT/m, 200 T/m/s at 3T). At 7T, a 32-channel head receive coil surrounded by a single-channel (circular-polarized) transmit coil was used. At 3T, the 52 head elements of a 64-channel head-neck receive coil were used. Image reconstruction was performed using the vendor-based implementation ("IcePAT") that applies 3D GRAPPA kernels and a prescan-based, virtual reference coil combination.[20] Unless stated otherwise, "EPI" refers to 3D-EPI and "GRE" refers to 3D-GRE in the remainder of this work.

At 7T, GRE protocols based on the recent multicenter, multivendor UK7T reproducibility study[21] were set up as listed below. All 7T scans were performed in sagittal slice orientation (x: head-feet, y: posterior-anterior) using nonselective narrow bandwidth RF pulses to suppress fat signal.[22] The vendor-provided 3D-GRE sequence was adapted to use the same image reconstruction as the SC-EPI. However, in accordance with the UK7T protocols for the Siemens MAGNETOM Terra 7T scanner,[23] all GRE scans used a zero CAIPIRINHA shift and "integrated" GRAPPA autocalibration scans (ACS). Flow compensation (along x and z) was only active for the single-TE GRE. The multi-TE GRE used a monopolar readout.

All EPI scans used fast initial FLASH ACS[24] and no flow compensation. The 0.7 mm single-TE EPI used integrated phase navigators for shot-by-shot phase correction, whereas all other EPI protocols used a one-time initial phase navigator for more efficient but static phase correction.[18]

The $x \times y$ field-of-view (FoV) was 224 mm × 224 mm for all scans, except for the UK7T-based multi-TE GRE (269 mm × 219 mm) and the high-resolution single-TE EPI (205 mm × 205 mm). The nominal flip angle was 15° for all 7T scans, except for the high-resolution multi-TE EPI (18°) to account a substantially longer TR. Only the latter used a phase partial Fourier (PF) factor of 6/8 and both blip-up (↑) and blip-down (↓) phase-encoding. Further protocol details are summarized in Table 1.

As small EPI factors ($N \leq 8$) tend to result in minor segmentation artifacts (Figure S2) and residual Nyquist ghosts seem negligible using "IcePAT" reconstruction, the 7T multi-echo EPI protocols ($N = 5, 6$) were performed with a single frequency-encode polarity for maximal acceleration. All scans were acquired with written informed consent from three subjects (I, II, and III) in accordance with the local ethics regulations. The following use cases of whole-head SC-EPI are examined and compared to the UK7T-based GRE protocols:

1. Faster QSM and R_2^* mapping at 7T:
   a. Single-TE at 0.7 mm isotropic resolution
   b. Multi-TE at 1.4 mm isotropic resolution
2. Higher-resolution QSM and R_2^* mapping at 7T:
   a. Single-TE at 0.4 mm isotropic resolution
   b. Multi-TE at 0.7 mm isotropic resolution
3. High-resolution QSM and R_2^* mapping at 3T:
   Multi-TE at 0.8 mm isotropic resolution

Experiments 1a and 1b provide ten times shorter acquisition times than the UK7T-based GRE protocols. For brevity, we refer to them as "fast" in the following. Experiments 2a and 2b provide 1/5 and 1/8 of the respective voxel volumes, while still being twice as fast. For brevity, we refer to them as "high-res." in the following.

Experiment 3 transfers the 7T high-resolution multi-TE EPI protocol to 3T for routine application in the Rhineland Study—a long-term, large-scale study in the general population[25] (https://www.rheinland-studie.de/en/). Unlike the 7T SC-EPIs, single-oblique axial slices (x: left-right, y: anterior-posterior) were acquired using slab-selective, binomial-121 water excitation with 20° nominal flip angle. A 216 mm × 216 mm $x \times y$ FoV

TABLE 1 Protocol parameters and preprocessing according to Figure 3.

	Single-TE experiments			Multi-TE experiments			
	GRE	Fast EPI	High-resolution EPI	GRE	Fast EPI	High-resolution EPI	3T EPI
Subject	**I**	**I**	**I**	**II**	**II**	**II**	**III**
Iso. voxel [mm]	0.7	0.7	0.4	1.4	1.4	0.7	0.8
Slices	224	240	420	120	120	240	176
Measurements	1	1-2[a,b]	1-2[a,b]	1	1[b]	1-2[b] / 3-4[c]	1-4[a,b] / 5-8[a,c]
TE [ms]	19	19	19	[4, 9, 14, 19, 24, 29, 34, 39]		[5.5, 14.5, 23.5, 32.5][d] [10.0, 19.0, 28.0, 37.0][e]	[7.4, 17.2, 27.0][d] [12.3, 22.1, 31.9][e]
TR [ms]	31	31	40	43	44	47	51.1
Parallel imaging	4×1	$3 \times 2_{z1}$	$1 \times 3_{z1}$	4×1	$3 \times 2_{z1}$	$3 \times 2_{z1}$	$3 \times 2_{z1}$
Seg/EPI f. (S/N)	—	9/12	31/17	—	11/5	14/6	10/ 7
Eff. acc. (R_{eff})	2.9[f]	36	25.5	2.3[f]	30	9	5.25
Phase PF	—	—	—	—	—	6/8	6/8
BW_x [Hz/mm]	100	1594	1630	260	1489	1489	1361
BW_y [Hz/mm]	—	75	82	—	194	146	116
TR_{vol} [min:s]	—	0:33	3:02	—	0:29	1:19	0:45
TA [min:s]	12:38	1:15[g]	6:14[g]	5:58	0:36[g]	5:32[h]	6:22[h]
Preprocessing	—	A→C→E	A→C→E	—	—	A→B→C→D→E	A→B→C→D→E

[a]Dual-polarity frequency-encoding measurements.
[b]Using blip-up phase-encoding.
[c]Using blip-down phase-encoding.
[d]"Jittered" TE set in odd-numbered measurements.
[e]"Jittered" TE set in even-numbered measurements.
[f]R_{eff} is reduced through integrated ACS acquisition.
[g]TA includes one initial FLASH ACS (one for all blip-up and one for all blip-down measurements).
[h]TA includes two initial FLASH ACS (one for all blip-up and one for all blip-down measurements).

is used. A 150-mm thick saturation slab, positioned below and parallel to the imaging slab and applied before each excitation, suppressed in-flowing blood signal. At 3T, both dual-polarity frequency-encoding and ↑ & ↓ phase-encoding were combined with two sets of "jittered" TEs, yielding $M = 8$ measurements in total, each with a $TR_{vol} = 45$ s. Further parameters are listed in Table 1.

At 3T, subject III was asked to lie still during a first iteration of all eight measurements and instructed to perform one realistic and one exaggerated motion during a second iteration of all eight measurements (see Figure S3). Realistic head motion was induced by moving the legs at about 1 min into the scan (during measurement 2, 0:56–1:41 min). For exaggerated head motion, subject III nodded slowly with a large amplitude at about 5 min into the scan (during measurement 7, 4:52–5:37 min).

3.2 | Preprocessing

The entire processing in this work was performed retrospectively based on DICOM magnitude and phase images reconstructed "online" (using the vendor "IcePAT" reconstruction). Only if a single SC-EPI image was acquired per TE, no further preprocessing was performed (fast multi-TE). Otherwise, an image-based preprocessing pipeline was implemented using standard software (e.g., FSL[26]) and custom basic python code (e.g., "phase matching" and "PF compensation") as outlined in Figure 3.

The minimal pipeline in this work consisted of motion correction (A, using the mcflirt and applyxfm4D methods implemented in FSL), and phase matching (C, see below) before data averaging (E). In an extended pipeline, the ↑ & ↓ phase-encoded images were used to estimate and correct for susceptibility-induced geometric distortions (B, using the topup and applytopup methods implemented in FSL). If dual-polarity frequency-encoding was applied, the final averaging step also corrected for residual Nyquist ghosts and segmentation artifacts. If phase partial Fourier sampling (PF) was combined with ↑ & ↓ phase-encoding, final averaging also compensated for PF-related blurring through appropriate k-space weighting (D, see below).

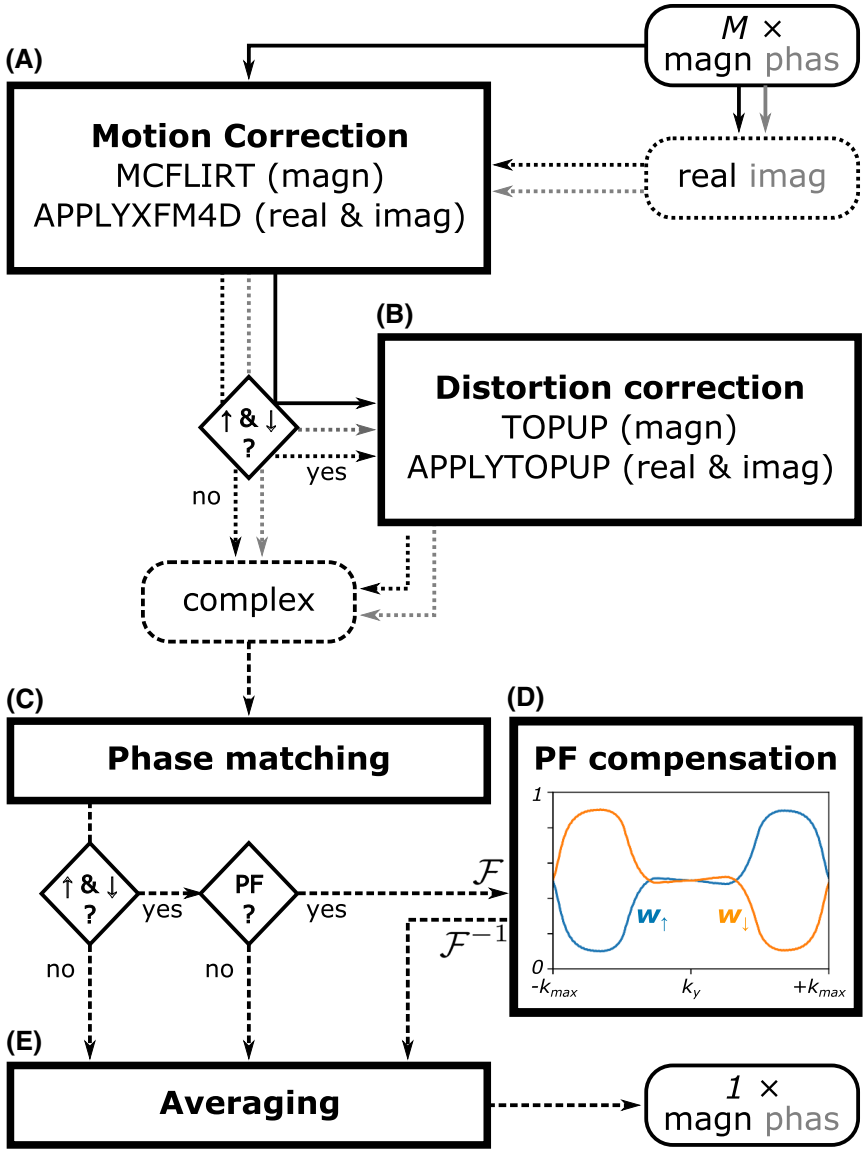

FIGURE 3 Preprocessing pipeline that turns M complex-valued native SC-EPI images into one complex-valued high-signal-noise-ratio (SNR) image per echo time (TE). The input images are retrospectively corrected for motion (A), geometric distortions (B) and phase changes (C). Finally, complex-valued averaging (E) is carried out to mitigate residual Nyquist ghosts and segmentation artifacts (if dual-polarity frequency-encoding was applied) and/or to compensate for partial Fourier (PF) blurring (D, if ↑ & ↓ phase-encoding was applied). Different complex image data formats are represented by line type. $\mathcal{F}$ and $\mathcal{F}^{-1}$: Fast Fourier transforms to k-space and back to image space.

3.2.1 | Phase matching

Local image phase changes over M repeated measurements were accounted for by matching the low spatial frequency contributions to the image phase with respect to the first measurement. For single-TE, this was carried out by subtracting a low-pass-filtered version of the phase changes (computed via the Hermitean-inner-product followed by a $2 \times 2 \times 2$-voxel Gaussian kernel smoothing of the real and imaginary images). For multi-TE data, the actual frequency changes over measurements were estimated as the changes of the phase difference between the first two rephased TEs divided by the TE spacing. Numerical integration of the low-pass-filtered frequency changes across measurements, multiplied with the respective TEs yielded consistent phase changes to be subtracted. For both single-TE and multi-TE data, this phase matching strategy keeps the high spatial frequency noise of the original complex-valued images unaltered while the image phases are aligned.

3.2.2 | Partial Fourier compensation

When phase PF sampling is combined with ↑ & ↓ phase-encoding, the ↑ and ↓ data, each collected $M/2$ times, are zero-filled at opposite k-space ends. Therefore, actual data is acquired $M/2$ times at each end and M times in the overlapping k-space section. Here, the images did not require individual PF reconstructions as compared to Reference 27. Instead, they were averaged using appropriate k-space weights in the style of Reference 27. For our data we found that smooth weights $w_\uparrow(k_y)$ and $w_\downarrow(k_y)$ resulted in better retrospective PF compensation than hard-coded weights (0, 0.5, 1) with sharp transitions. This is primarily due to the tapering involved in the preceding,

zero-filled PF reconstruction. We derived the weights from the ↑ and ↓ k-space magnitudes themselves, following temporary Fourier-transform of the images to k-space, as

$$w_{\uparrow}(k_y) = \frac{f_{\uparrow}(k_y)}{f_{\uparrow}(k_y) + f_{\downarrow}(k_y)}, \quad w_{\downarrow}(k_y) = \frac{f_{\downarrow}(k_y)}{f_{\uparrow}(k_y) + f_{\downarrow}(k_y)}.$$

Herein, the high-SNR k-space magnitude functions $f_{\uparrow/\downarrow}$ were obtained by root-sum-of-squares combination of the actual k-space signals $s_{\uparrow/\downarrow}$ across all k_x, k_z, TE_j and repeated measurements (m),

$$f_{\uparrow/\downarrow}(k_y) = \sqrt{\sum_m \sum_j \sum_{k_z} \sum_{k_x} |s_{\uparrow/\downarrow}(k_x, k_y, k_z, \mathrm{TE}_j, m)|^2}.$$

The resulting PF compensation weights were therefore consistent for all averages and TEs (examples shown in Figure 3D).

3.2.3 | Complex-valued nonlocal means denoising

As a final, optional step, we applied a complex-valued customization of a nonlocal means denoising algorithm.[28] Here, the ANTsPy[29] implementation was applied separately on temporary high-pass-filtered real and imaginary images obtained by first subtracting a Gaussian-smoothed baseline phase ($4 \times 4 \times 4$-voxel kernel applied to unwrapped phase) and then linearly mapping the corresponding real and imaginary values $\in [-4096, 4096]$ to positive values $\in [0, 4096]$. Air voxels were excluded from denoising (first image magnitude quintile). After mapping the denoised high-frequency images back to the range $[-4096, 4096]$, the smooth baseline phase, assumed to have very little low-frequency noise, was added back to the denoised complex data. In this work, denoising was only applied to the 0.4 mm isotropic single-TE data at 7T and to the 0.8 mm isotropic multi-TE data at 3T prior to R_2^* fitting.

3.3 | SWI, QSM, and R_2^* mapping

As a purely magnitude-based multi-TE summary image, the root-mean-squares combinations across TEs (RMS) was computed and compared, where applicable.

Susceptibility-weighted images[30] were computed from the preprocessed magnitude and phase images considering all TEs using CLEAR-SWI[31] (https://github.com/korbinian90/CLEARSWI.jl). For all SWI data, minimum intensity projections (MIP) across 5.6 mm axial slabs are also presented in this work.

For QSM, the phase images for each measurement and TE were unwrapped using a 3D best path algorithm[32] divided by $2\pi \cdot \mathrm{TE}_j$ [s] to obtain the Larmor frequency variation in Hz. The latter were combined across TEs for multi-TE data ($\mathrm{TE}_j \leq 19$ms at 7T, all TE_j at 3T). Background field contributions were removed using Variable-radius Sophisticated Harmonic Artifact Reduction for Phase data.[33,34] Susceptibility mapping was performed based on the Variable-radius Sophisticated Harmonic Artifact Reduction for Phase data-processed frequency maps using Homogeneity Enabled Incremental Dipole Inversion (HEIDI).[35] All susceptibility values were referenced to the average susceptibility of brain tissue within the FoV.[36]

R_2^* mapping was performed on all multi-TE magnitude images using the NUMerical Algorithm for Real-time T_2^* mapping (NumART_2^*)[37] (https://github.com/korbinian90/MriResearchTools.jl).

4 | RESULTS

Figure 4 shows several views of the single-TE magnitude data at 7T and corresponding SWIs and MIPs. The preprocessing of both EPI scans consisted of motion correction and phase matching between the two DPAs. The 0.4-mm isotropic results are also shown after final complex-valued nonlocal means denoising of the average. In comparison to the GRE, the 0.7-mm EPI reveals less distinct signal voids as indicated in the temporal cerebellar white matter, in the posterior lobe of the cerebellum and above the sphenoidal sinus (magenta arrow). In addition, the GRE image exhibits flow artifacts (e.g., cyan arrow) and the 0.7-mm EPI images appear crisper as indicated, for instance, by the more detailed depiction of white matter draining veins. Exquisite details are captured by the 0.4-mm scan that are even more pronounced after denoising.

Magnified views of the corresponding quantitative susceptibility maps are shown in Figure 5. Maps at 0.4-mm isotropic resolution are additionally shown with denoising prior to susceptibility mapping. Apart from more restrictive masking required for the GRE data (especially in the cerebellum), the susceptibility maps of the GRE and EPI data are nearly identical with additional fine details at 0.4 mm.

Figure 6 shows unilateral axial views of the multi-TE magnitude images at 7T and magnified views of the corresponding SWIs and MIPs. As the 1.4-mm EPI data consisted of a single measurement, only the 0.7-mm EPI data underwent preprocessing, which consisted of motion correction, phase matching, and distortion correction between the two ↑ & ↓ measurements per "jittered" TE. The RMS images are near identical for the 1.4-mm EPI and

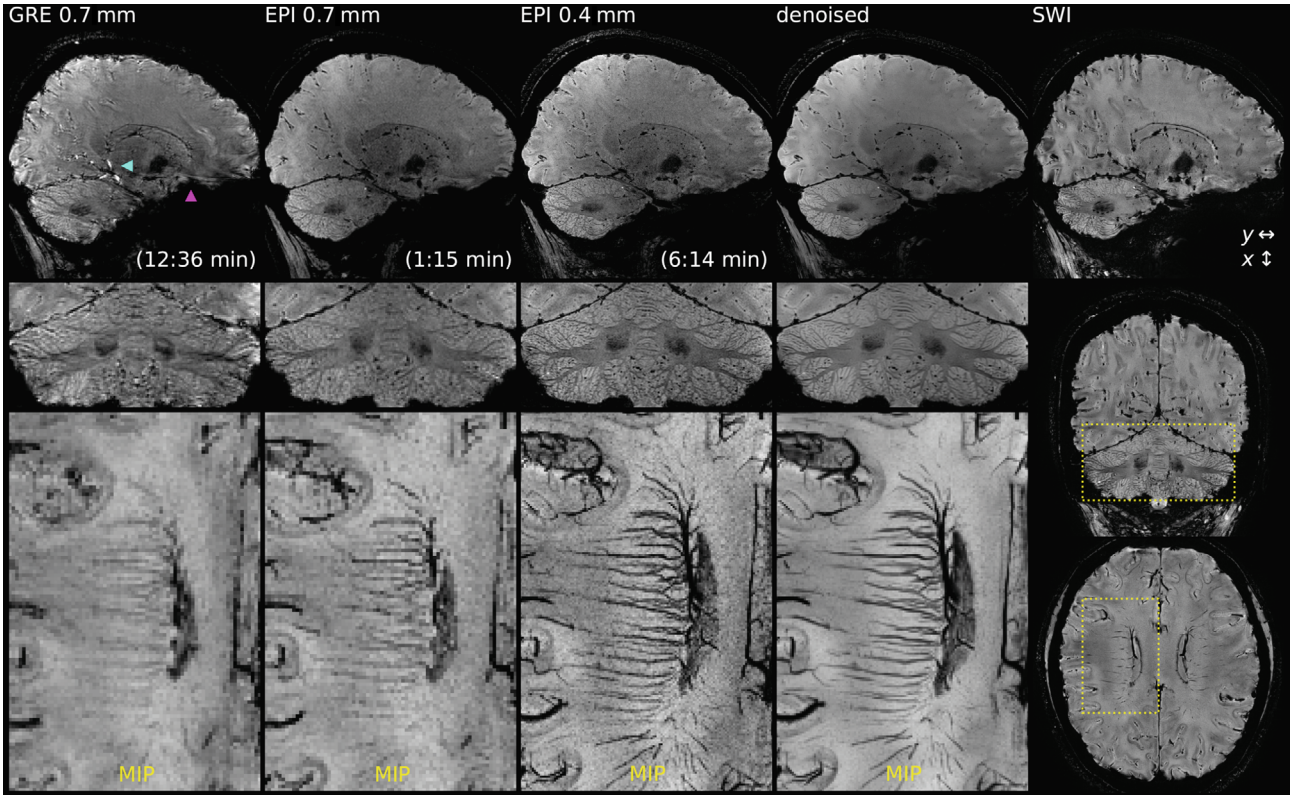

FIGURE 4 Whole-head sagittal views and magnified coronal views of the preprocessed magnitude images (top) at native resolution from single-echo time (TE) experiments according to Table 1. Right: whole-head SWI of denoised 0.4-mm EPI. Bottom: magnified axial minimum intensity projections (MIP) across 5.6 mm of the SWI images.

GRE. In addition to the preprocessed 0.7-mm RMS, the corresponding 0.7-mm RMS using only ↑ phase-encoding is shown (red frame). Yellow arrows point to small structures that, accordingly, demonstrate improved resolution after complete preprocessing, including PF compensation.

Magnified views of the corresponding R_2^* maps and quantitative susceptibility maps are shown in Figure 7. The GRE susceptibility map shows artifacts in the cerebellum (cyan arrows) and both GRE and EPI susceptibility maps at 1.4-mm resolution show increased values in the axial view above the sphenoidal sinus, just like the corresponding R_2^* maps (magenta arrows). With EPI, eight times smaller cubic voxels (0.7 mm) could be collected in about the same TA as the GRE (1.4 mm). The 0.7-mm data resolves more details and reduces signal dropouts, signal fluctuations and ultimately quantitative mapping errors compared to the 1.4-mm GRE data.

Finally, Figure 8 shows unilateral axial views of the 3T multi-TE magnitude images, corresponding SWIs and MIPs, resulting R_2^* and susceptibility maps for two iterations of the 0.8mm EPI protocol. Figure S3B shows that moderate motion artifacts were present in the raw images of measurements 2 and 8 and substantial motion artifacts in the raw images of measurement 7 of the second iteration. Image data of measurement 7 was replaced by a copy of measurement 5 data before further preprocessing, which is equivalent to motion censoring in this context. Preprocessing of the two iterations consisted of motion correction, phase matching, and distortion correction before averaging. For the three TEs acquired in measurements 1, 3, 5, 7 of the second iteration, only partial mitigation of segmentation artifacts can be achieved due to motion-censoring of measurement 7. Still, results after preprocessing are comparable to the minimal motion iteration with complete mitigation, although slightly reduced in SNR (see top two rows of Figure 8). The bottom row shows average images and maps of the same data (after motion censoring of measurement 7) without preprocessing. Detail level and overall quality of the susceptibility map without preprocessing is degraded. Notably, reduced image magnitudes, in particular for long TEs with increasing phase discrepancies between averages, result in a substantial upwards bias of R_2^* across the whole brain.

5 | DISCUSSION

5.1 | Experimental data

The fast single-TE SC-EPI data was effectively $R_y \cdot R_z \cdot N/M = 36$-fold accelerated (each dual-polarity

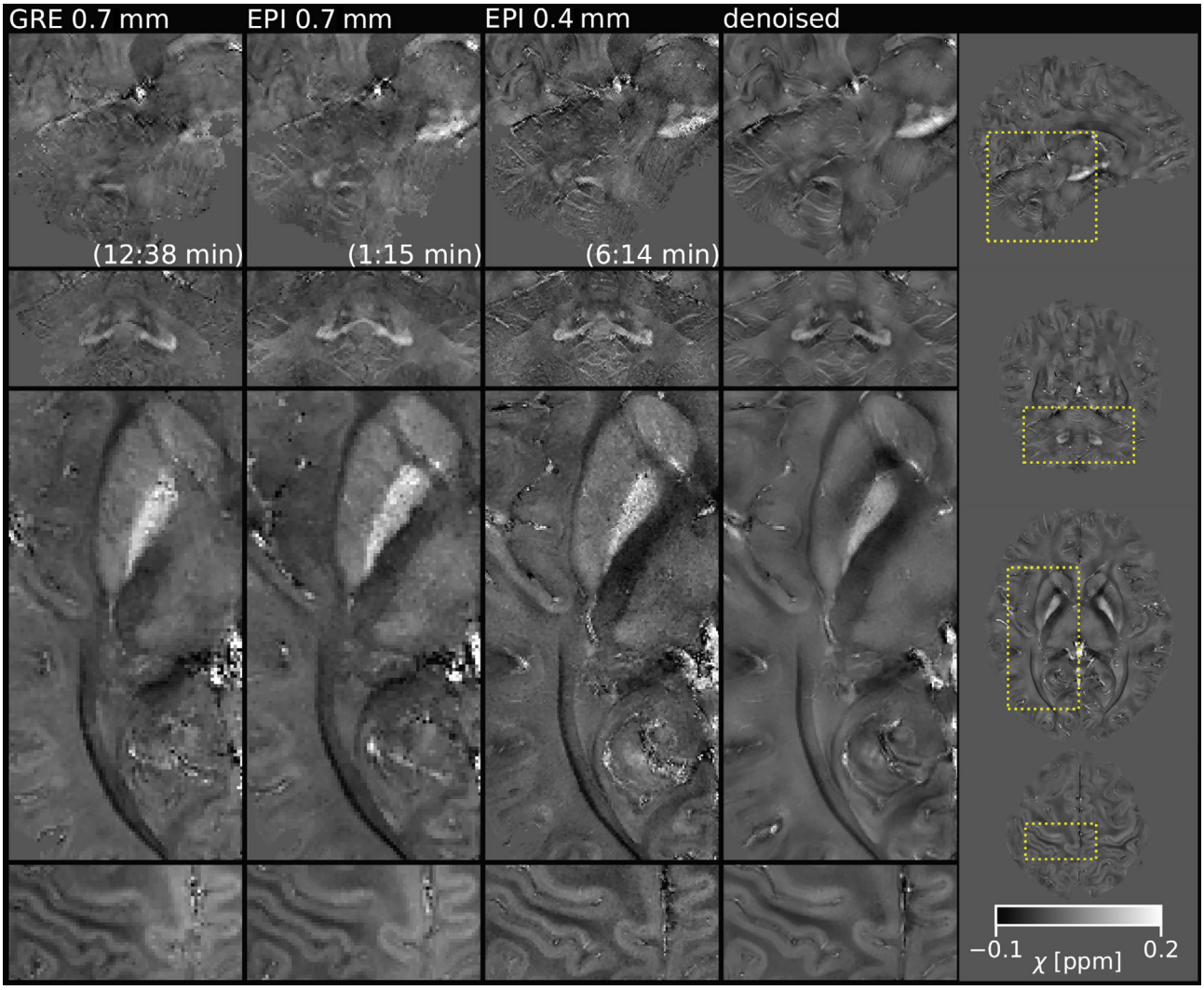

FIGURE 5 Magnified views of the susceptibility maps at native resolution from single-TE experiments according to Table 1. The two top rows show sagittal and coronal views of the pons, red nucleus, substancia nigra, cerebellum and dentate nucleus. The two bottom rows show axial views of the striatum, the optic tract, the primary motor and somatosensory cortex. The right panel, showing whole-head views of susceptibility obtained from 0.4-mm data after denoising, indicates the magnified areas.

measurement 72-fold) and thus about ten times faster (1:15 min including external FLASH ACS[24]) than the $R_y = 4$-fold undersampled, UK7T-based GRE reference (12:38 min including time-consuming integrated ACS). Magnitude images are even improved and susceptibility maps are near identical. In addition to reduced artifacts due to less intra-volume motion and field variations, no flow artifacts are visible in the 0.7mm EPI magnitude compared to the 0.7mm GRE magnitude. For 3D-GRE imaging using partial flow compensation (only along x and z according to the UK7T protocol reference), such flow artifacts can be expected.[38] On the other hand, segmented EPI is known to exhibit a different type of flow artifact,[39] which was, however, not observed here.

The increased resolution of the 0.4-mm SC-EPI resulted in less dropouts and showed even more remarkable details compared to the 0.7mm SC-EPI, particularly of the convoluted structures of the cerebellar cortex. The increased amount and length of the medullary veins projected by the 0.4 mm susceptibility-weighted MIP also demonstrates substantially reduced partial volume effects by 1/5 of the original voxel volume. Finer details due to increased resolution and reduced sensitivity to motion with SC-EPI are also depicted in the resulting susceptibility maps of Figure 5. In particular, layers of the cortical gray matter, deep gray matter structures, cerebral white matter and even fine white matter tracts in the pons can be delineated (see Video S1 for whole-head axial views).

Despite substantially increased resolution, much shorter acquisition times per measurement (TR_{vol}=3:02 min) could be achieved for the ultra-highly resolved SC-EPI with 400 microns isotropic voxels compared to

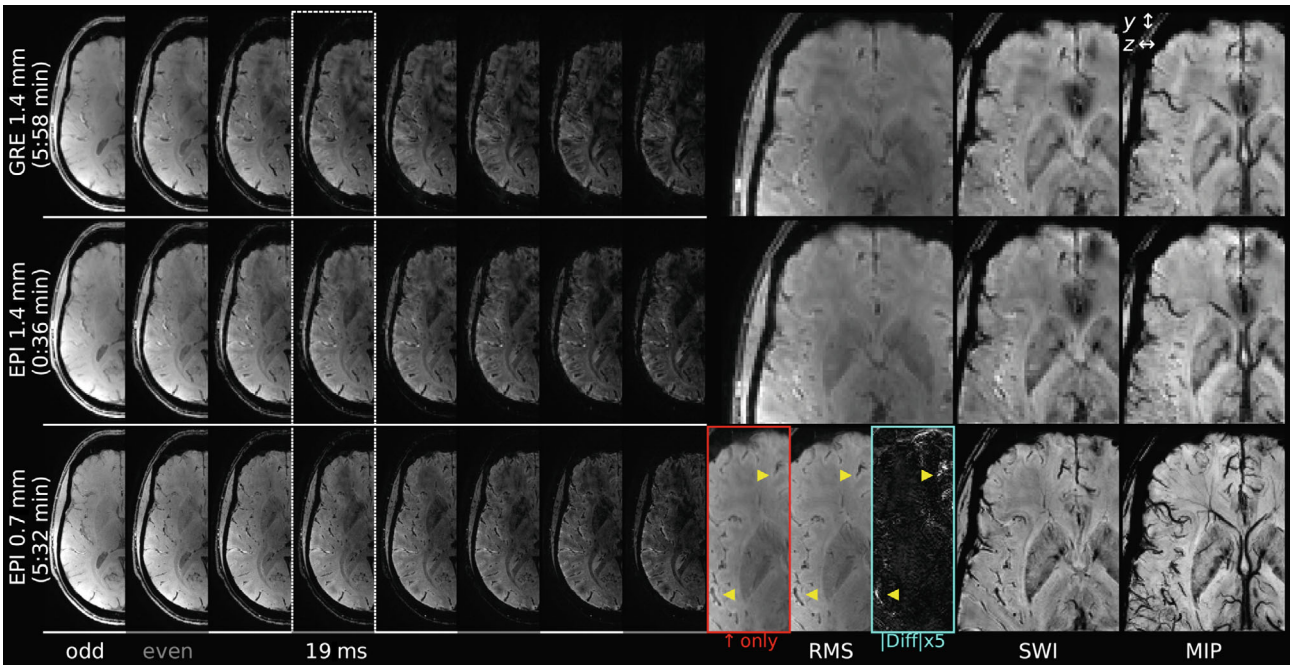

FIGURE 6 Unilateral, axial views of all echo time (TE) magnitude images at native resolution from multi-TE experiments according to Table 1. Top rows: one measurement each, bottom row: two averages per TE, preprocessed. TE = 19 ms is included in all sets (dotted frame). Odd- and even-numbered measurements (interleaved sets of "jittered TEs") are indicated by white and gray lines, respectively. Right columns: magnified axial views of the RMS, SWI and corresponding 5.6mm MIP. Yellow arrows indicate improved resolution after preprocessing compared to the ↑ only RMS (red frame), highlighted by the absolute difference image (cyan frame).

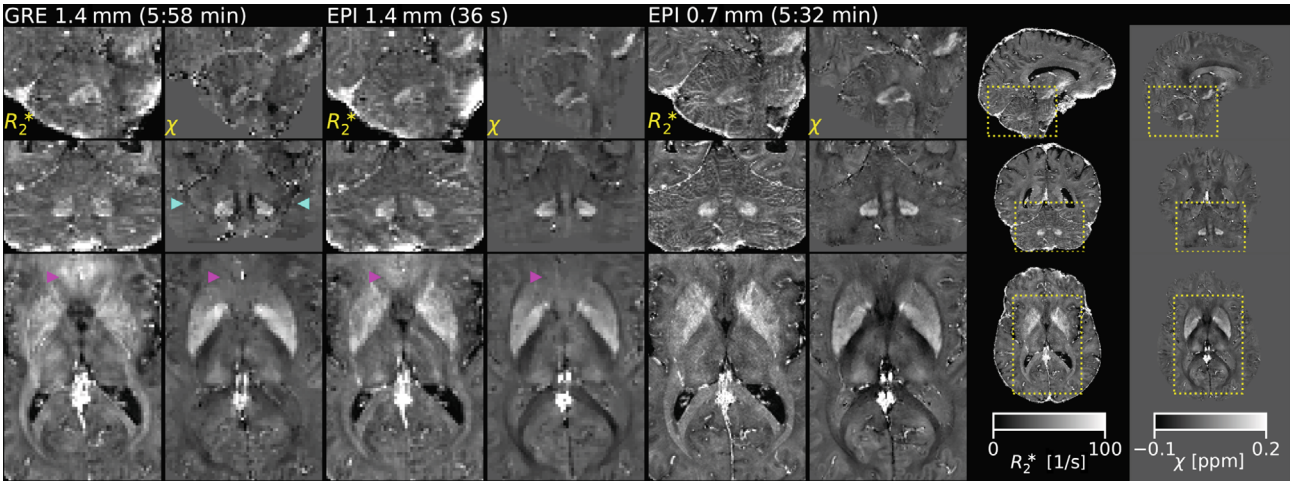

FIGURE 7 Magnified sagittal, coronal and axial views of the 7T R_2^* maps and susceptibility maps from multi-echo time (TE) experiments according to Table 1. Eight times smaller cubic voxels (0.7mm) in about the same acquisition times as the gradient echo (1.4 mm) reduce quantitative mapping errors in highly off-resonant areas (magenta arrows). The right panels, showing whole-head maps of the 0.7 mm EPI, indicate the magnified areas.

the 0.7mm GRE reference (TA = 12:38 min). For sufficient SNR, only two averages were necessary (TA = 6:14 min), still resulting in less than half of the TA of the 0.7mm GRE. Figure S4 demonstrates that similar acquisitions are feasible in TA = 5:33 min. A corresponding 400 microns GRE with identical TR, parallel imaging and ACS would be about $N/M = 8.5$ times longer (approximately 46-52 minutes). According to Figure S4, still about 34 minutes were needed (or only a 22.4-mm slab was covered within the same TA), if the GRE TR was minimized.

A single 1.4-mm isotropic multi-TE SC-EPI measurement yielded comparable data quality to the

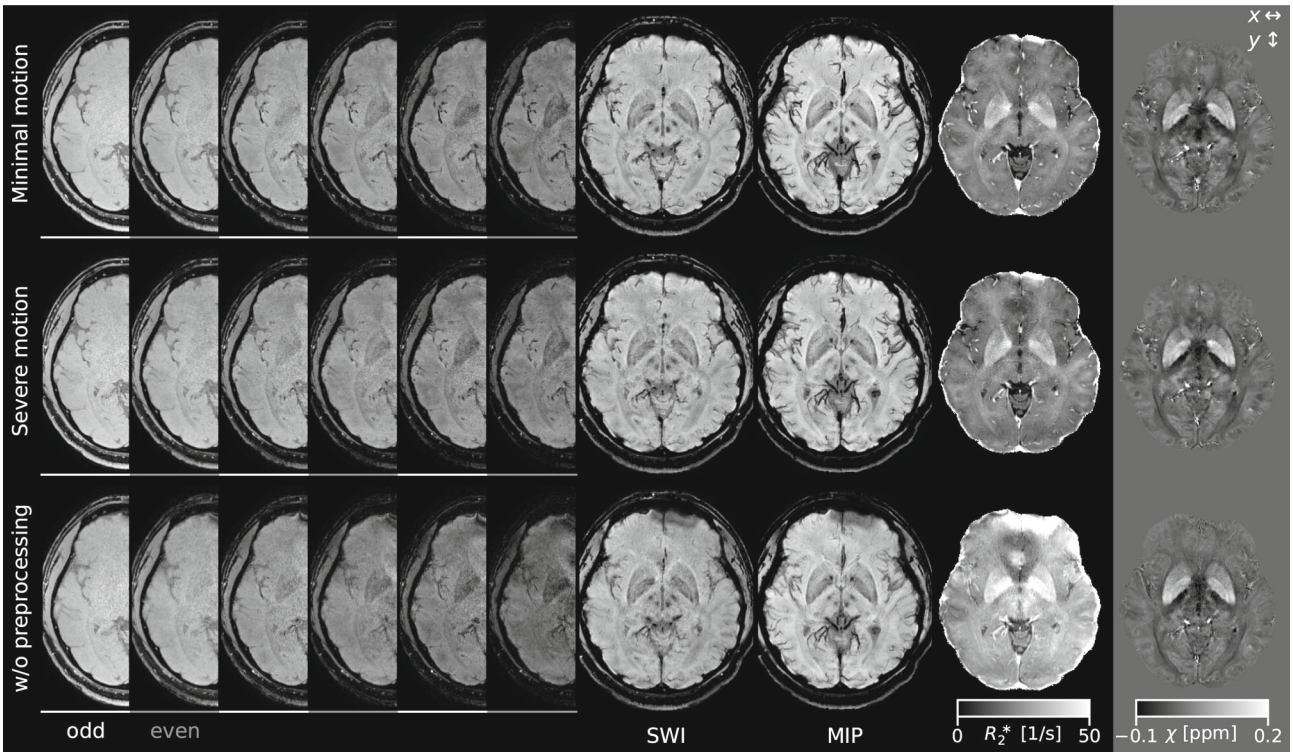

FIGURE 8 Unilateral, axial views of the magnitude images for all echo times (TEs) of the 3T experiments (0.8mm isotropic, acquisition time = 6:22) after complete preprocessing with minimal (top row, 4 averages per TE) and with severe head motion (middle row, 3/4 averages per odd/even-numbered TE due to motion censoring of measurement 7; cf. Figure S3). Bottom row: same data averaged without preprocessing (only linear phase differences in x direction removed). Odd- and even-numbered measurements (TEs) are indicated by white and gray lines, respectively. Right columns: axial views of the SWI and MIP, R_2^* map (after denoising) and susceptibility map (without denoising). Correction added after online publication 1 August 2024. The authors have updated Figure 8 to correct quality issues introduced during the publication process.

corresponding multi-TE GRE reference in about one tenth of the scan time, as demonstrated in Figure 6. In approximately the same scan time as the 1.4-mm multi-TE GRE (and only half of the scan time of the 0.7mm single-TE GRE), whole-head multi-TE SC-EPI data at 0.7mm isotropic resolution with no apparent distortion was obtained. Hereby, our implemented PF compensation restored resolution that was originally compromised by zero-filling in the individual measurement data. Overall, significantly smaller voxels and reduced motion and field variation per measurement resulted in less signal dropouts and reduced artifacts and allows to resolve much finer details compared to the 1.4-mm resolution. Furthermore, it translated to substantially improved R_2^* and susceptibility maps as shown in Figure 7.

Similar conclusions can be drawn from the multi-TE experiments performed at 3T, as demonstrated in Figure 8. Due to particularly short acquisition times per measurement (TR_{vol} = 45 s), intra-volume motion sensitivity was rather small. In the presence of severe head motion (middle row), retrospective inter-volume motion correction and phase matching produced nearly similar quality as with negligible, unintentional motion (top row). Without preprocessing (bottom row), displacements and predominantly motion-induced phase discrepancies caused blurring, phase errors and severe magnitude reduction. In particular, R_2^* maps are substantially affected by an upwards bias, if phase matching before averaging is omitted. With all retrospective, image-based corrections applied, however, clear SWIs, MIPs and quantitative maps were obtained from the SC-EPI scans.

5.2 | Proposed methods

The degrees of freedom through repeated measurements may be used in various ways. Here, only pragmatic processing was done, that was applicable retrospectively on already reconstructed images using readily available software.

In particular the 0.8-mm multi-TE SC-EPI data, acquired at 3T over eight, already motion-insensitive measurements of only 45 s duration each, benefited from retrospective motion correction, distortion correction, phase matching, partial Fourier compensation and mitigation of (minimal) segmentation artifacts. In addition, motion censoring was feasible. Together with the other retrospective

corrections, the quality of the outcome was substantially improved. This is particularly useful for study participants with difficulties to lie still (see Figure 8). The four measurements of 0.7-mm multi-TE SC-EPI data acquired at 7T (1:19 min each) benefited from a similar pipeline (excluding mitigation of segmentation artfacts, see below). Even the two single-TE SC-EPI measurements at 0.7 mm (33 s each) and 0.4-mm isotropic resolution (3:02 min each) allowed for retrospective inter-volume motion correction and phase matching in addition to mitigating segmentation artifacts. Coregistration before averaging is particularly useful at isotropic resolutions as high as 400 microns.[40] However, prospective intra-volume motion and phase correction would be even more beneficial. A corresponding GRE scan of about 30–50 min duration would only be feasible with prospective motion correction.

In this work, GRE protocols based on the multivendor UK7T study[21] have been used as an established reference at 7T. However, GRE sequences and protocols can be optimized as well, for instance by implementing CAIPI sampling, using external FLASH ACS, oblique axial slice orientation, or bipolar multi-echo frequency-encoding with phase correction.[41] Either way, neither a single-echo GRE nor a single-echo EPI sampling window should be longer than tissue T_2^* to minimize blurring.[15] The efficiency-optimal $TR_{opt} > T_2^*$ should therefore not be exceeded, despite the slow decline of SNR efficiency for $TR > TR_{opt}$ (Figure 1). Multi-TE images (small EPI factors) with TEs up to 40ms or longer, on the other hand, could be acquired particularly efficiently without suffering from such T_2^* blurring. Still, only TEs < 32 ms were used at 3T in this work to meet the strict TA < 7 min requirement of the Rhineland study.

5.3 | Related methods

Recently proposed echo planar k-t-space sampling techniques[42–44] benefit from increased SNR efficiency using $TR > T_2^*$ as well. While multi-TE EPI and echo planar time-resolved imaging (EPTI),[42] for instance, share some features, they differ particularly in the k_y-t-space subsampling (cf. Fig. 1B,E in Reference 42). This allows EPTI to apply sophisticated reconstruction of distortion-minimized images at high TE-resolution (and more complex signal-time-dependencies[44]). Nevertheless, by sampling the k_y-t space along very steep trajectories, the highly-segmented multi-TE experiments of this work provided images with comparable TE-resolution (4.5–5 ms) within comparable TA (comparable number of required shots)[42] using standard image reconstruction.

The proposed DPA technique has a lot in common with previously proposed Nyquist ghost correction or related methods.[45–47] Dual-polarity GRAPPA,[48] for instance, uses dual-polarity calibration scans to optimize GRAPPA kernels for k-space lines that are systematically shifted against each other. Our main objective was the mitigation of off-resonance-induced segmentation artifacts caused by k-space phase jumps that occur even without system imperfections. Only coincidentally, various polarity-dependent image phase artifacts (e.g., eddy currents-induced) are reduced as well through plain cancelation, albeit at the cost of doubled scan time. Nevertheless, future applications may benefit additionally from methods like dual-polarity GRAPPA, for example, to reduce polarity-dependent artifacts after incomplete cancelation (cf. 3T motion experiment).

We found that interleaved multishot EPIs with only few echo sections (e.g. $N = 5–7$ for the multi-TE experiments) generally do not seem to suffer as severely from off-resonance-induced segmentation artifacts as EPIs with larger N, which makes DPA optional (cf. Figures S2 and S5). This might be due to fewer off-resonance phase jumps that are further apart in k-space compared to an intermediate number of echo sections (e.g., 12 or 17 in the single-TE experiments). Corresponding image artifacts are more localized (see Figure S2) and less pronounced as less phase is accumulated over shorter EPI readouts (smaller phase error tilt[19]).

In our high-resolution multi-TE scans, we used reversed phase-encoding in repeated measurements. This allowed us to compensate for PF-related resolution loss and to correct for susceptibility-induced geometric distortions in addition to inter-volume motion and phase changes. However, only small PF-related resolution loss and geometric distortions were observed in our highly segmented images (see magnified RMS comparison to ↑ only RMS in Figure 6). The same applies to the 3T protocol. Upon distortion correction, no geometric mismatch with a conventional T_1-weighted anatomical scan was visible (see Figure S6).

The reversed phase-encoding approach is closely related to the 3D blip-up/blip-down acquisition (BUDA) that has recently been utilized successfully for QSM[49] and R_2^* mapping.[50] BUDA can potentially take even more advantage of the scanning speed by acquiring complementary sampling patterns per blip-up and blip-down shot. Compared to BUDA applications proposed thus far, this work relies on moderate parallel imaging undersampling for both phase-encode directions and rather small distortions at much higher spatial resolutions, as facilitated through strong interleaved multishot segmentation. Still, future applications could also benefit from advanced BUDA acquisition and image reconstruction.

Importantly, the image-based, retrospective correction strategy followed here makes the proposed acquisition

and correction approach very accessible. The use of CAIPIRINHA sampling is not even mandatory with reduced undersampling,[14,15] and therefore, it is even compatible with more basic image reconstruction. Figures S7A-C demonstrate consistent and high-quality results using the methods of this work. Note that the complex-valued denoising step is generally considered optional and the user should be aware that subtle structures may get blurred (see Figure S7A). Even without retrospective corrections, averaging or denoising, 1 mm isotropic or anisotropic SWI or R_2^* mapping well below 1 min scan time could be performed in clinical settings. In research settings, more elaborate methods or improved hardware, including parallel transmission flip angle homogenization[51] or more powerful imaging gradient systems,[52] can be used in addition or alternatively without diminishing our main findings.

6 | CONCLUSIONS

Interleaved multishot 3D-EPI is highly SNR-efficient and well suited for high-resolution single-TE and multi-TE gradient echo imaging at high and ultra-high fields. Single scans are acquired rapidly, making them relatively motion-insensitive and providing many degrees of freedom to further increase robustness against experimental imperfections over repeated short measurements. Therefore, interleaved multishot 3D-EPI, with or without CAIPIRINHA sampling, readily allows for rapid and robust QSM and R_2^* mapping at 7 and 3T.

ACKNOWLEDGMENTS

We want to thank Mohammad Shahid for the nipype implemention of the extended preprocessing pipeline for the Rhineland study and Philipp Ehses for valuable discussions.

CONFLICT OF INTEREST STATEMENT

The authors declare no potential conflict of interests.

DATA AVAILABILITY STATEMENT

Separate nipype pipelines for basic and for extended preprocessing are shared under https://github.com/mrphysics-bonn/ep3d-highres-preprocessing (short hash at time of submission: `26704e0`). The skipped-CAIPI 3D-EPI sequence can be accessed via the Siemens C2P exchange platform at https://webclient.us.api.teamplay.siemens-healthineers.com/c2p (`v2.0` at time of submission).

ORCID

Rüdiger Stirnberg https://orcid.org/0000-0001-7021-1063
Andreas Deistung https://orcid.org/0000-0002-2427-1302
Jürgen R. Reichenbach https://orcid.org/0000-0002-2640-0630
Monique M. B. Breteler https://orcid.org/0000-0002-0626-9305
Tony Stöcker https://orcid.org/0000-0002-8946-9141

REFERENCES

1. Langkammer C, Schweser F, Krebs N, et al. Quantitative susceptibility mapping (QSM) as a means to measure brain iron? *A* post mortem validation study. *NeuroImage*. 2012;62:1593-1599.
2. Hametner S, Endmayr V, Deistung A, et al. The influence of brain iron and myelin on magnetic susceptibility and effective transverse relaxation - a biochemical and histological validation study. *Neuroimage*. 2018;179:117-133.
3. Stüber C, Morawski M, Schäfer A, et al. Myelin and iron concentration in the human brain: a quantitative study of MRI contrast. *Neuroimage*. 2014;93:95-106.
4. Chen J, Gong NJ, Chaim KT, Otaduy MCG, Liu C. Decompose quantitative susceptibility mapping (QSM) to sub-voxel diamagnetic and paramagnetic components based on gradient-Echo MRI data. *Neuroimage*. 2021;242:118477.
5. Dimov AV, Gillen KM, Nguyen TD, et al. Magnetic susceptibility source separation solely from gradient Echo data: histological validation. *Tomography*. 2022;8:1544-1551.
6. Dimov AV, Nguyen TD, Gillen KM, et al. Susceptibility source separation from gradient echo data using magnitude decay modeling. *J Neuroimaging*. 2022;32:852-859.
7. Pruessmann KP, Weiger M, Scheidegger MB, Boesiger P. SENSE: sensitivity encoding for fast MRI. *Magn Reson Med*. 1999;42:952-962.
8. Griswold MA, Jakob PM, Heidemann RM, et al. Generalized autocalibrating partially parallel acquisitions (GRAPPA). *Magn Reson Med*. 2002;47:1202-1210.
9. Breuer FA, Blaimer M, Mueller MF, et al. Controlled aliasing in volumetric parallel imaging (2D CAIPIRINHA). *Magn Reson Med*. 2006;55:549-556.
10. Sun H, Wilman AH. Quantitative susceptibility mapping using single-shot Echo-planar imaging. *Magn Reson Med*. 2015;73:1932-1938.
11. Poser BA, Koopmans PJ, Witzel T, Wald LL, Barth M. Three dimensional echo-planar imaging at 7 tesla. *Neuroimage*. 2010;51:261-266.
12. Langkammer C, Bredies K, Poser BA, et al. Fast quantitative susceptibility mapping using 3D EPI and Total generalized variation. *Neuroimage*. 2015;111:622-630.
13. Stäb D, Bollmann S, Langkammer C, Bredies K, Barth M. Accelerated mapping of magnetic susceptibility using 3D planes-on-a-paddlewheel (POP) EPI at ultra-high field strength. *NMR Biomed*. 2017;30:e3620.
14. Sati P, Thomasson DM, Li N, et al. Rapid, high-resolution, whole-brain, susceptibility-based MRI of multiple sclerosis. *Mult Scler J*. 2014;20:1464-1470.
15. Zwanenburg JJM, Versluis MJ, Luijten PR, Petridou N. Fast high resolution whole brain T2* weighted imaging using Echo planar imaging at 7T. *Neuroimage*. 2011;56:1902-1907.

16. Wang D, Ehses P, Stöcker T, Stirnberg R. Reproducibility of rapid multi-parameter mapping at 3T and 7T with highly segmented and accelerated 3D-EPI. *Magn Reson Med*. 2022;88:2217-2232.
17. Marques JP, Khabipova D, Gruetter R. Studying Cyto and Myeloarchitecture of the human cortex at ultra-high field with quantitative imaging: R1, R2* and magnetic susceptibility. *Neuroimage*. 2017;147:152-163.
18. Stirnberg R, Stöcker T. Segmented K-space blipped-controlled aliasing in parallel imaging for high spatiotemporal resolution EPI. *Magn Reson Med*. 2021;85:1540-1551.
19. Feinberg DA, Oshio K. Phase errors in multi-shot Echo planar imaging. *Magn Reson Med*. 1994;32:535-539.
20. Jellúš V, Kannengiesser SAR. Adaptive coil combination using a body coil scan as phase reference. *Proceedings of the International Society of Magnetic Resonance in Medicine*. Vol 23. ISMRM; 2014.
21. Rua C, Clarke WT, Driver ID, et al. Multi-centre, multi-vendor reproducibility of 7T QSM and R2* in the human brain: results from the UK7T study. *Neuroimage*. 2020;223:117358.
22. Stirnberg R, Brenner D, Stöcker T, Shah NJ. Rapid fat suppression for three-dimensional Echo planar imaging with minimized specific absorption rate. *Magn Reson Med*. 2016;76:1517-1523.
23. Clarke W. UK7T network harmonized neuroimaging protocols. 2018 https://ora.ox.ac.uk/objects/uuid:55ca977f-62df-4cbf-b300-2dc893e36647. Accessed September 23, 2023.
24. Ivanov D, Barth M, Uludağ K, Poser BA. Robust ACS acquisition for 3D Echo planar imaging. *Proceedings of the International Society of Magnetic Resonance in Medicine*. Vol 23. ISMRM; 2015:2059.
25. Breteler MMB, Stöcker T, Pracht E, Brenner D, Stirnberg R. MRI in the Rhineland study: a novel protocol for population neuroimaging. *Alzheimers Dement*. 2014;10:P92.
26. Jenkinson M, Beckmann CF, Behrens TEJ, Woolrich MW, Smith SM. Fsl. *Neuroimage*. 2012;62:782-790.
27. Koopmans PJ, Pfaffenrot V. Enhanced POCS reconstruction for partial Fourier imaging in multi-Echo and Time-series acquisitions. *Magn Reson Med*. 2021;85:140-151.
28. Manjón JV, Coupé P, Martí-Bonmatí L, Collins DL, Robles M. Adaptive non-local means Denoising of MR images with spatially varying noise levels. *J Magn Reson Imaging*. 2010;31:192-203.
29. Tustison NJ, Cook PA, Holbrook AJ, et al. The ANTsX ecosystem for quantitative biological and medical imaging. *Sci Rep*. 2021;11:9068.
30. Haacke EM, Xu Y, Cheng Y-CN, Reichenbach JR. Susceptibility weighted imaging (SWI). *Magn Reson Med*. 2004;52:612-618.
31. Eckstein K, Bachrata B, Hangel G, et al. Improved susceptibility weighted imaging at ultra-high field using bipolar multi-Echo Acquisition and optimized image processing: CLEAR-SWI. *Neuroimage*. 2021;237:118175.
32. Abdul-Rahman HS, Gdeisat MA, Burton DR, Lalor MJ, Lilley F, Moore CJ. Fast and robust three-dimensional best path phase unwrapping algorithm. *Appl Optics*. 2007;46:6623-6635.
33. Schweser F, Deistung A, Lehr BW, Reichenbach JR. Quantitative imaging of intrinsic magnetic tissue properties using MRI signal phase: an approach to in vivo brain iron metabolism? *Neuroimage*. 2011;54:2789-2807.
34. Wu B, Li W, Guidon A, Liu C. Whole brain susceptibility mapping using compressed sensing. *Magn Reson Med*. 2012;67:137-147.
35. Schweser F, Sommer K, Deistung A, Reichenbach JR. Quantitative susceptibility mapping for investigating subtle susceptibility variations in the human brain. *Neuroimage*. 2012;62:2083-2100.
36. Deistung A, Schweser F, Reichenbach JR. Overview of quantitative susceptibility mapping. *NMR Biomed*. 2017;30:e3569.
37. Hagberg GE, Indovina I, Sanes JN, Posse S. Real-time quantification of T2* changes using multiecho planar imaging and numerical methods. *Magn Reson Med*. 2002;48:877-882.
38. Deistung A, Dittrich E, Sedlacik J, Rauscher A, Reichenbach JR. ToF-SWI: simultaneous time of flight and fully flow compensated susceptibility weighted imaging. *J Magn Reson Imaging*. 2009;29:1478-1484.
39. Beck G, Li D, Haacke EM, Noll TG, Schad LR. Reducing oblique flow effects in interleaved EPI with a centric reordering technique. *Magn Reson Med*. 2001;45:623-629.
40. Lüsebrink F, Sciarra A, Mattern H, Yakupov R, Speck O. T1-weighted in vivo human whole brain MRI dataset with an ultrahigh isotropic resolution of 250 *M*m. *Sci Data*. 2017;4:170032.
41. Eckstein K, Dymerska B, Bachrata B, et al. Computationally efficient combination of multi-channel phase data from multi-echo acquisitions (ASPIRE). *Magn Reson Med*. 2018;79:2996-3006.
42. Wang F, Dong Z, Reese TG, et al. Echo planar time-resolved imaging (EPTI). *Magn Reson Med*. 2019;81:3599-3615.
43. Guo R, Zhao Y, Li Y, et al. Simultaneous QSM and metabolic imaging of the brain using SPICE: further improvements in data acquisition and processing. *Magn Reson Med*. 2021;85:970-977.
44. Wang F, Dong Z, Reese TG, Rosen B, Wald LL, Setsompop K. 3D Echo planar time-resolved imaging (3D-EPTI) for ultrafast multi-parametric quantitative MRI. *Neuroimage*. 2022;250:118963.
45. Chen NK, Wyrwicz AM. Removal of EPI Nyquist ghost Artifacts with two-dimensional phase correction. *Magn Reson Med*. 2004;51:1247-1253.
46. Xiang QS, Ye FQ. Correction for geometric distortion and N/2 ghosting in EPI by phase Labeling for additional coordinate encoding (PLACE). *Magn Reson Med*. 2007;57:731-741.
47. Xie VB, Lyu M, Liu Y, Feng Y, Wu EX. Robust EPI Nyquist ghost removal by incorporating phase error correction with sensitivity encoding (PEC-SENSE). *Magn Reson Med*. 2018;79:943-951.
48. Hoge WS, Polimeni JR. Dual-polarity GRAPPA for simultaneous reconstruction and ghost correction of Echo planar imaging data. *Magn Reson Med*. 2016;76:32-44.
49. Bilgic B, Poser BA, Langkammer C, Setsompop K, Liao C. 3D-BUDA enables rapid distortion-free QSM acquisition. *Proceedings of the International Society of Magnetic Resonance in Medicine*. ISMRM; 2020:596.
50. Chen Z, Liao C, Cao X, et al. 3D-EPI blip-up/down acquisition (BUDA) with CAIPI and joint Hankel structured low-rank reconstruction for rapid distortion-free high-resolution T2* mapping. *Magn Reson Med*. 2023;89:1961-1974.
51. Daniel L, Pracht Eberhard D, Rüdiger S, Patrick L, Tony S. Interleaved binomial kT-points for water-selective imaging at 7T. *Magn Reson Med*. 2022;88:2564-2572.
52. Feinberg DA, Beckett AJ, Vu AT, et al. Next-generation MRI scanner designed for ultra-high-resolution human brain imaging at 7 tesla. *Nat Methods*. 2023;20:2048-2057.

53. Deichmann R, Adolf H, Nöth U, Kuchenbrod E, Schwarzbauer C, Haase A. Calculation of signal intensities in hybrid sequences for fast NMR imaging. *Magn Reson Med*. 1995;34:481-489.

SUPPORTING INFORMATION

Additional supporting information may be found in the online version of the article at the publisher's website.

Figure S1. Numerical phantom simulations of dual-polarity frequency-encoding for increasing off-resonance frequencies, Δf (96 phase-encode lines, segmentation factor $S = 8$, EPI factor = echo sections $N = 96/S = 12$). Segmentation artifacts are clearly visible in the individual dual-polarity images (+ and -) for 440Hz and 880Hz off-resonance frequencies that are mitigated through dual-polarity averaging. Additional, massive off-resonance aliasing without echo time shifting (w/o ETS) does not disappear through dual-polarity averaging (not shown).

Figure S2. Numerical phantom simulations of dual-polarity averaging (with ETS) in accordance to Figure S1 for varying segmentation (S) and EPI factors (N) while maintaining $TE = 19$ms in the k-space center (note the decreasing TE range with decreasing N). For simplicity, only the resulting magnitude images for both polarity acquisitions and the dual-polarity average are shown. Note: the two right-most circles approximately represent the largest realistic proton frequencies at 3T and 7T close to the chemical shift of fat. As EPI factors (number of echo sections) get smaller ($N \leq 8$), artifacts in the individual polarity images become negligible for more typical off-resonance frequencies when compared to the dual-polarity average.

Figure S3. Axial SC-EPI magnitude views with "jittered" multi-TE measurements of two iterations of the 3T Rhineland Study QSM/R_2^* protocol. The EPI trajectories displayed to the left of each rephased multi-TE set indicate the respective frequency (k_x) and phase-encode (k_y) polarity. The first protocol iteration (A) has been acquired without substantial head motion. During the second iteration (B), the subject was instructed to reposition the legs once (implying realistic motion) and to nod with the head once strongly (exaggerated motion). Measurements 2 (orange frame) and 7 (red frame) were affected, respectively. Apart from additional, involuntary motion artifacts in measurement 8 (orange frame), all other scans were found normal.

Figure S4. Alternative 400 microns isotropic scans at 7T, each with TE=19 ms using 3-fold parallel imaging undersampling (from top to bottom): the vendor 3D-GRE sequence with non-selective excitation, head-feet frequency-encoding (BW_x=175 Hz/mm) and minimized TR=29 ms (approx. 34 min TA); the vendor 3D-GRE sequence with slab-selective excitation (22.4 mm + 14.3% slice oversampling) and frequency-encoding (BW_x=200 Hz/mm) along a reduced left-right FoV (166 mm) and minimized TR = 30 ms (approx. 5.5 min TA); the proposed 3D-EPI sequence with non-selective excitation, head-feet frequency-encoding ($BW_x = 1630$ Hz/mm), minimized TR and dual-polarity averaging (approx. 5.5 min TA). Compared to the 400 microns protocol discussed in the main text, the following changes have been made to scan even more efficiently: $S = 30$ ($BW_y = 81$ Hz/mm), TR = 40 ms, 414 slices. Note substantially reduced artifacts related to motion and B_0 changes compared to the whole-brain vendor 3D-GRE protocol.

Figure S5. Raw images vs. average images demonstrate mitigation of off-resonance-induced segmentation artifacts in all dual-polarity SC-EPI scans at 7T using medium large EPI factors (rows 1-2), and negligible segmentation artifacts in multi-TE scans at 7T (rows 3-4) and 3T (row 5) using small EPI factors. Slices that should show most prominent off-resonance artifacts were selected. Yet, clear segmentation artifacts are only visible in rows 1-2 (stripe patterns, framed yellow and magnified). The fourth column additionally shows the shortest TE of all multi-TE images as a guidance to distinguish reduced signal-dropouts from other off-resonance artifacts.

Figure S6. SC-EPI average magnitude images at the shortest TE compared to a conventional T1-weighted anatomical image (T1w, native isotropic resolution: 1mm in rows 1-2, 0.8mm in rows 3-5). Gray/white matter boundaries were derived from the T1w by thresholding after coregistration (mutual information) and interpolation (sinc) to the SC-EPI. The SC-EPIs of rows 1-3 did not undergo geometric distortion correction. Yet, minor geometric mismatch to T1w is only apparent in the magnified views of row 2 and 3 (third column).

Figure S7. Approximate reproduction of paper Figures 4, 6 and 8 using three different subjects to demonstrate consistent results with the proposed methods (same subject in A and B; two different Rhineland study participants in C: one with minimal and one with substantial motion, however not requiring motion censoring). In (A), the more time-efficient 400 microns protocol from Figure S4 has been used. Additionally, it has been acquired three more times to yield a four-fold high-SNR average using the proposed minimal pipeline with 8 instead of 2 dual-polarity averages. Not least due to the retrospective motion correction involved, a few additional fine structures can be appreciated in the high-SNR average SWI minimum intensity projection compared to the denoised version of the single average (cyan arrows). This demonstrates the limitations of the optional, phase-preserving NLM denoising step.

Video S1. Axial views across the whole head at 400 microns isotropic. SWIs, MIPs (across 5.6 mm) and

susceptibility maps are based on nonlocal means-denoised SC-EPI data.

How to cite this article: Stirnberg R, Deistung A, Reichenbach JR, Breteler MMB, Stöcker T. Rapid submillimeter QSM and R_2 mapping using interleaved multishot 3D-EPI at 7 and 3 Tesla. *Magn Reson Med*. 2024;92:2294-2311. doi: 10.1002/mrm.30216

APPENDIX A. SNR-EFFICIENT SAMPLING OF A FREE-INDUCTION DECAY

Regardless of the GRE sequence type, sampling of a single free-induction decay (FID) can be considered. The SNR is proportional to the Fourier series DC coefficient divided by the noise standard deviation.[53]

Figure A1A,B defines the sequence timing assumed for the FID model. Over the sampling window, $\tau(\mathrm{TR})$, the steady-state signal $S_0 = S(t = 0, \mathrm{TR}, \alpha)$ shall be weighted by a generic signal envelope, $f(t)$. Assuming Gaussian noise with a variance of σ^2 yields the following SNR equation:

$$\begin{aligned}\mathrm{SNR} &= c \cdot \frac{\frac{1}{\tau(\mathrm{TR})}\int_{\delta_0}^{\mathrm{TR}-\delta_1} S_0 \cdot f(t)dt}{\sigma\sqrt{\frac{\tau_0}{\tau(\mathrm{TR})}}} \\ &= \frac{S_0}{\sigma} \cdot Q_f(\mathrm{TR}, \delta_0, \delta_1) \quad .\end{aligned} \tag{A1}$$

The receive bandwidth factor $\sqrt{\tau_0/\tau}$ scales the noise standard deviation (τ_0: arbitrary normalization) and the global factor c accounts for all other factors that scale the signal magnitude. These factors are incorporated in the "quality factor"[53] together with the cumulative signal over the sampling window:

$$Q_f(\mathrm{TR}, \delta_0, \delta_1) = \frac{c}{\sqrt{\tau(\mathrm{TR})\tau_0}}\int_0^{\tau(\mathrm{TR})} f(\delta_0 + t)dt.$$

The quality factor of a monoexponential $f_{\mathrm{FID}}(t) = e^{-tR_2^*}$ is

$$Q_{\mathrm{FID}}(\mathrm{TR}, \delta_0, \delta_1) = \frac{c \cdot e^{-\delta_0 R_2^*}}{R_2^*\sqrt{\tau_0}} \cdot \frac{1 - e^{-\tau(\mathrm{TR})R_2^*}}{\sqrt{\tau(\mathrm{TR})}}. \tag{A2}$$

Substituting the steady-state signal using the Ernst angle,

$$S_0 = \sqrt{\tanh\left(\frac{R_1\mathrm{TR}}{2}\right)} \approx \sqrt{\frac{R_1\mathrm{TR}}{2}}, \text{ if } \frac{R_1\mathrm{TR}}{2} \ll 1, \tag{A3}$$

into Equation (A1), the sampled FID SNR efficiency becomes:

$$\frac{\mathrm{SNR}(\mathrm{TR}, \delta_0, \delta_1)}{\sqrt{\mathrm{TR}}} \approx \frac{Q_{\mathrm{FID}}(\mathrm{TR}, \delta_0, \delta_1)}{\sigma\sqrt{2\mathrm{T}_1}}. \tag{A4}$$

Solving $\partial Q_{\mathrm{FID}}/\partial \mathrm{TR}|_{\mathrm{TR}_{\mathrm{opt}}} = 0$ yields

$$2(\mathrm{TR}_{\mathrm{opt}} - \delta_0 - \delta_1)R_2^* = e^{(\mathrm{TR}_{\mathrm{opt}}-\delta_0-\delta_1)R_2^*} - 1,$$

which is satisfied by the efficiency-optimal $\mathrm{TR}_{\mathrm{opt}}$

$$\mathrm{TR}_{\mathrm{opt}} \approx 1.256\mathrm{T}_2^* + \delta_0 + \delta_1. \tag{A5}$$

The peak efficiency is obtained by substituting Q_{FID} according to Equation (A2) with $\mathrm{TR}_{\mathrm{opt}}$ into Equation (A4):

$$\frac{\mathrm{SNR}(\mathrm{TR}_{\mathrm{opt}}, \delta_0, \delta_1)}{\sqrt{\mathrm{TR}_{\mathrm{opt}}}} \approx \frac{0.451c}{\sigma\sqrt{\tau_0}} \cdot e^{-\delta_0/\mathrm{T}_2^*}\sqrt{\frac{\mathrm{T}_2^*}{\mathrm{T}_1}} \tag{A6}$$

APPENDIX B. SNR-EFFICIENT SAMPLING OF ME-GRE-TYPE SEQUENCES

If, according to Figure A1 C, we assume a fraction $0 \leq \dot{\delta} \leq 1$ of the FID sampling window interspersed over a split sampling window of reduced cumulative time, $\tau_N(\mathrm{TR}) = \tau[1 - \dot{\delta}]$, instead of Equation (A2) one finds

$$\begin{aligned}&Q_N(\mathrm{TR}, \delta_0, \delta_1, \dot{\delta}, N) \\ &= \frac{c}{\sqrt{\tau_N(\mathrm{TR})\tau_0}} \cdot \sum_{n=0}^{N-1}\int_{\frac{\tau(\mathrm{TR})}{N}n}^{\frac{\tau(\mathrm{TR})}{N}(n+1-\dot{\delta})} e^{-(\delta_0+t)R_2^*}dt \\ &= \frac{c \cdot e^{-\delta_0 R_2^*}}{R_2^*\sqrt{\tau_N(\mathrm{TR})\tau_0}}\left[1 - e^{-\frac{\tau(\mathrm{TR})}{N}[1-\dot{\delta}]R_2^*}\right]\sum_{n=0}^{N-1} e^{-\tau(\mathrm{TR})R_2^*\frac{n}{N}} \\ &= \frac{c \cdot e^{-\delta_0 R_2^*}}{R_2^*\sqrt{\tau_N(\mathrm{TR})\tau_0}}\left[1 - e^{-\frac{\tau(\mathrm{TR})}{N}[1-\dot{\delta}]R_2^*}\right]\frac{1 - e^{-\tau(\mathrm{TR})R_2^*}}{1 - e^{-\frac{\tau(\mathrm{TR})}{N}R_2^*}} \\ &= \frac{Q_{\mathrm{FID}}(\mathrm{TR}, \delta_0, \delta_1)}{\sqrt{1 - \dot{\delta}}} \cdot \frac{1 - e^{-\frac{\tau(\mathrm{TR})}{N}R_2^*[1-\dot{\delta}]}}{1 - e^{-\frac{\tau(\mathrm{TR})}{N}R_2^*}},\end{aligned}$$

which has the coherent special cases:

$$\begin{aligned}&\lim_{\dot{\delta}\to 1} Q_N = 0 \\ &\lim_{\dot{\delta}\to 0} Q_N = Q_{\mathrm{FID}}(\mathrm{TR}, \delta_0, \delta_1) \\ &\lim_{N\to 1} Q_N = e^{-\dot{\delta}\delta_0 R_2^*} Q_{\mathrm{FID}}\left(\mathrm{TR}[1 - \dot{\delta}], \delta_0[1 - \dot{\delta}], \delta_1[1 - \dot{\delta}]\right) \\ &\lim_{N\to\infty} Q_N = \sqrt{1 - \dot{\delta}} \cdot Q_{\mathrm{FID}}(\mathrm{TR}, \delta_0, \delta_1).\end{aligned}$$

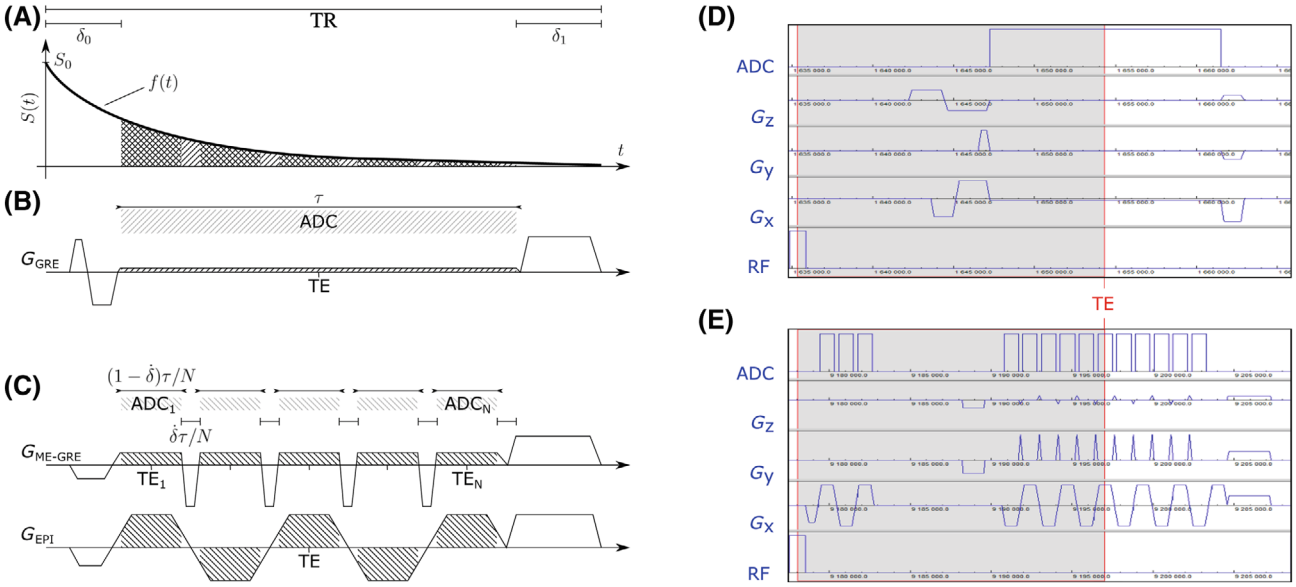

FIGURE A1 Illustration of the sampling parameters assumed for signal-noise-ratio (SNR) efficiency calculations (A). Representative frequency-encode pulse sequences for the contiguous FID model (B; e.g. GRE with flow compensated dephaser in δ_0) and for the split FID sequence model (C; monopolar multi-TE GRE or multi-shot EPI with $N = 5$ echoes each). Right: One example TR of actual pulse sequence simulations for the GRE (D) and EPI (E) single-TE experiment according to Table 1. ADC: analog-to-digital conversion of the sampled signal.

Corresponding limits apply to the SNR efficiency:

$$\frac{\mathrm{SNR}_N(\mathrm{TR}, \delta_0, \delta_1, \dot{\delta}, N)}{\sqrt{\mathrm{TR}}} \approx \frac{Q_N(\mathrm{TR}, \delta_0, \delta_1, \dot{\delta}, N)}{\sigma\sqrt{2\mathrm{T}_1}}.$$

The first two cases are trivial. The third case corresponds to a single signal acquisition interval, just like the FID model. However, the sampling window is shorter by $\dot{\delta}\tau/N$ (Figure A1B,C). The efficiency-optimal $\mathrm{TR}_{N\to 1} = (\mathrm{TR}_{\mathrm{opt}} - \delta_0 - \delta_1)/[1-\dot{\delta}] + \delta_0 + \delta_1$ is increased accordingly, but the peak SNR efficiency is identical to the FID model.

The last case is the upper limit for many acquisition intervals (e.g., single-shot EPI). The efficiency-optimal $\mathrm{TR}_{N\to\infty} = \mathrm{TR}_{\mathrm{opt}}$ is the same as for the FID. However, the peak SNR efficiency is scaled down by $\sqrt{1-\dot{\delta}}$.

Figure A1D,E depicts actual pulse sequence examples for the FID model and the multi-echo model, respectively. The examples correspond to the 0.7 mm single-TE GRE and EPI protocols according to Table 1.